Diamond & Related Materials 122 (2022) 108775

Contents lists available at ScienceDirect

Diamond & Related Materials

journal homepage: www.elsevier.com/locate/diamond

Controlling the carrier density of surface conductive diamond

M.W. Geis [a,*], M.A. Hollis [a], G.W. Turner [a], J. Daulton [a], J.O. Varghese [a], K. Klyukin [b], J. Wang [b], B. Yildiz [b], B. Zhang [a]

[a] Lincoln Laboratory, Massachusetts Institute of Technology, Lexington, MA, USA
[b] Massachusetts Institute of Technology, Cambridge, MA, USA

ARTICLE INFO

Keywords:
Diamond
H-terminated
Surface conduction
Carrier density
Crystal step

ABSTRACT

By placing a diamond in a H_2 plasma and exposing it to air or overcoating it with Al_2O_3/SiO_2, evaporated WO_3, or other transition metal oxides a 2 dimensional, 2D, conductive hole gas forms on the diamond surface. Field effect transistors, FETs, made using this 2 D hole gas have the potential of replacing GaN FETs for use in high-power switching and high-frequency power applications. To achieve this goal, it is necessary to control the hole carrier density. When the carrier density is too high the device cannot be turned off and will have a low operational drain voltage due to electric-field break-down of diamond. On the other hand, too low a carrier density results in limited drain current, reduced power handling capability, and high on resistance. For diamond surface FETs using Al_2O_3/SiO_2 as a gate oxide a carrier density between 1×10^{13} to 6×10^{13} cm^{-2} is the most desirable, depending on the intended operating voltage and the drain current density.

This article discusses H-terminated procedure to controllably vary the carrier density from 1×10^{13} to 6×10^{13} cm^{-2}. This is accomplished by varying the H-termination parameters; temperature, termination time, H_2 pressure, and the microwave plasma power. During termination the diamond surface is etched and the density and type of crystal sets that form on the diamond surface is determined by these parameters. A model is presented of how the crystal step density and their character, single and double steps, can affect the carrier density.

1. Introduction

While O-terminated diamond is insulating, when the same surface is H terminated in a plasma formed in H_2 it becomes conductive, as discovered by Landstrass in 1989 [1]. After many years of research it was generally agreed that the conduction was the result of transfer doping [2] where electrons leave the diamond and bind to materials deposited or adsorbed from the air on the diamond substrate. When electrons leave the diamond a positive layer of holes form in the diamond at its surface, which is mobile and makes a p-type conductive surface. Crawford [3] has a detailed discussion of the history of transfer doping. Several review articles have been published on the electrical properties of surface conductive diamond [2–5] including FETs operating >2500 V [6].

Two semiconductor properties, carrier density, D, and mobility, μ, determine many of the characteristics of the surface field effect transistor, FET. The on resistance, R, is inversely related to the product of the carrier density and mobility, $R = 1/D\mu$. The carrier density times the saturated velocity determines the maximum drain current, and the maximum operating voltage of the FET is inversely related to the carrier density. Control of the carrier density is crucial to match a diamond FET performance to specific an application. This article reports on controlling carrier density by varying the temperature, and H-termination parameters: time, microwave plasma power, and H_2 pressure. The experiments discussed here were inspired by Stallcup and Perez's report [7] on the effect of diamond's temperature during H-terminate on crystal step formation.

2. Experiment

(100) diamond substrates used with these experiments were 7 × 7 mm, 300 μm thick, and offcut 5 to 6° to the [011]. To obtain reproduceable results the diamond and the plasma chamber used for H termination were cleared of impurities, Na, K, and non-diamond C [8].

2.1. H-termination recipes

H-termination recipes, shown in Fig. 1, consist of three steps;

* Corresponding author.
E-mail address: geis@ll.mit.edu (M.W. Geis).

https://doi.org/10.1016/j.diamond.2021.108775
Received 23 September 2021; Received in revised form 29 November 2021; Accepted 8 December 2021
Available online 15 December 2021

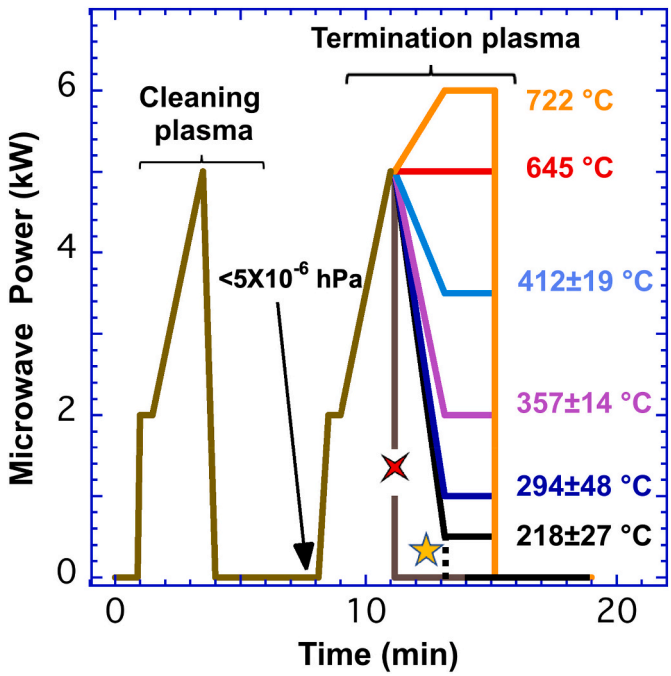

Fig. 1. Microwave plasma power as a function of time and diamond temperatures during the last 2 min of termination for six H-termination recipes. Two additional nonstandard recipes are shown by a red four-pointed star and a yellow five-pointed star. The green power curve is the same for all recipes and each recipe has its own color that is used in the following graphs to indicate the recipe for that data point. Measurements of the diamond temperatures are discussed in Appendix A.

- Step 1. Plasma cleaning to remove gasses adsorbed on the diamond and chamber walls.

The cleaning consists of pumping the chamber containing the diamond to $<5 \times 10^{-6}$ hPa, $<3.8 \times 10^{-6}$ Torr, back filling with 15 Torr of H_2, and forming a plasma with 2 kW of microwave plasma power. The power and pressure are increased over a 2 min period to 145 Torr and 5 kW and then immediately the power is shut off. The chamber is then again pumped to $<5 \times 10^{-6}$ hPa.

- Step 2. Establishing a consistent diamond surface for H-termination experiments.

As in step 1 a 145 Torr, 5 kW plasma is generated and the pressure and power are held constant for 10 s.

- Step 3. Experimental recipes.

After the 10 s in step 2, one of 6 standard H-termination recipes were performed. They consist of ramps to the desired pressure and power levels over a 2 min period, which are then maintained at that pressure and power for an additional 2 min, after which the power is shutoff and the diamond is removed. See Fig. 1. Two additional nonstandard recipes were performed where the power is terminated after the 10 s in step 2 and the other where the power and pressure are ramped to 0.5 kW and 15 Torr in 2 min, after which the power is terminated. These 2 recipes are indicated by the red four-pointed star and the yellow five-pointed star respectively in Fig. 1. Details of the microwave powers, pressures, diamond temperature, and optical emission are given in Appendix A.

2.2. Atomic layer deposition

Once removed from the chamber the diamond is transported in dry nitrogen to an atomic layer deposition, ALD, unit where approximately 18 nm of Al_2O_3/SiO_2 is deposited on the diamond [9]. Details of the ALD deposition are given in Appendix B. After ALD the surface resistance decreases over time when exposed to air. A delay time between ALD and electrical measurements of >3 days was used to ensure a stable resistance is recorded [8].

3. Experimental results

The resulting carrier density, determined by Hall measurements, increases with the microwave power and diamond temperature for each recipe, as shown in Fig. 2. With the increase in microwave power the concentration of H atoms increases, which is discussed in Appendix A. A linear fit to the data is shown in Fig. 2 along with its equation. The estimated errors for the equation's coefficients were calculated from the data without considering the estimated errors in the actual measurements. For the two nonstandard recipes where the power to the plasma was abruptly shut off after 10 s at 5 kW and after a 2 min ramp to 0.5 kW, the carrier densities are within the experimental error of the red recipe where the microwave power was maintained at 5 kW for 4 min and 10 s with a temperature of 645 °C. Since the diamond is offcut 5 to 6° to the [011], it exhibits anisotropic resistance with the lowest resistance along the $[0\bar{1}1]$ direction and the highest resistance along the [011] direction. This is the result of a higher carrier mobility along the crystal steps in the $[0\bar{1}1]$ direction [8]. The *van-der-Pauw ratio*, shown in Fig. 3, is the van-der-Pauw-measured resistance with the current flowing along the [011] direction divided by the measured resistance with the current flowing along the $[0\bar{1}1]$ direction. These measured resistances are not the actual resistance along the [011] and $[0\bar{1}1]$ directions. The actual resistances along the [011], $R_{[011]}$, and $[0\bar{1}1]$, $R_{[0\bar{1}1]}$, directions can be calculated from these van-der-Pauw measurements and are approximated by the (eq.)

$$R_{[011]}/R_{[0\bar{1}1]} = (van - der - Pauw\ ratio)^{0.3} \quad \text{(eq.)}$$

For a *van-der-Pauw ratio* of ten the ratio of the actual resistances, $R_{[011]}/R_{[0\bar{1}1]}$, is approximately two. Appendix C describes the resistance measurement using van-der-Pauw structure and more detailed

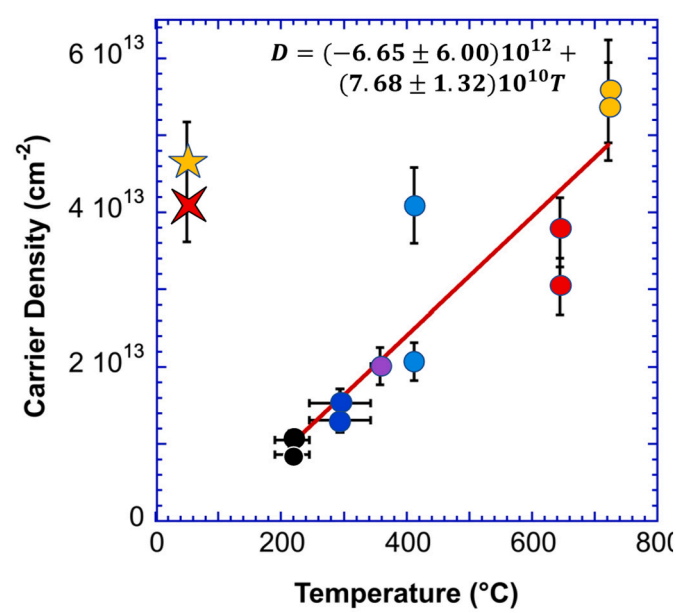

Fig. 2. Carrier density as a function of the diamond temperature for the last 2 min of termination for each recipe. The line and the equation are a linear fit to the data, with D being the carrier density as a function of T, the temperature. Note that the carrier densities for the nonstandard recipes, four and five pointed star symbols, do not follow the curve, but have comparable carrier densities to the red 5-kW 645 °C recipe. The Table in Appendix D contains the data for this and the following graphs.

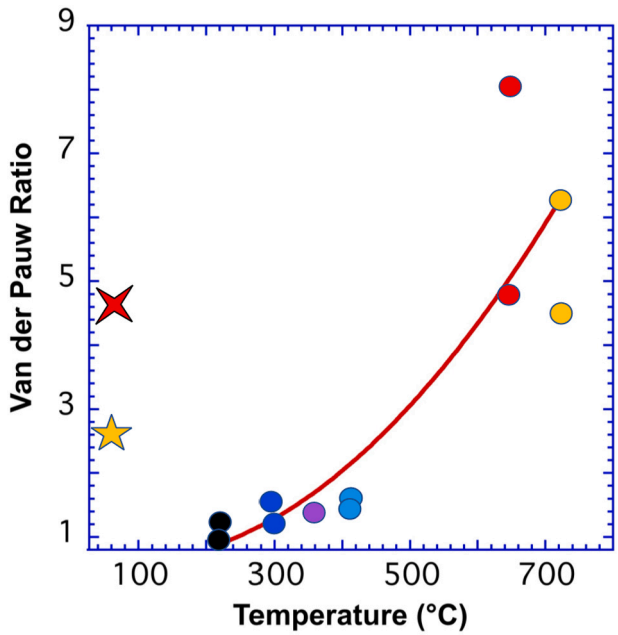

Fig. 3. Van-der-Pauw ratio as a function of diamond temperature during the last 2 min of termination. The curve is a second order polynomial fit to the data. The Table in Appendix D contains the data for this graph.

calculations can be obtained in references [8,10,11] As the microwave power increases with each recipe, the surface resistance decreases for both $R_{[011]}$ and $R_{[0\bar{1}1]}$, with $R_{[0\bar{1}1]}$ always being less than $R_{[011]}$, as shown Fig. 4. Line curves and equations to fit $R_{[011]}$ and $R_{[0\bar{1}1]}$ data are shown in Fig. 4. Fig. 5 shows the carrier mobility in the $[0\bar{1}1]$ direction as a function of carrier density. The mobility generally decreases with increasing carrier density. A power fit to the data has the mobility proportional to the carrier density to the -0.25 ± 0.10 power. For comparison the dotted curve is the mobility as a function of carrier density for H-terminated air-activated diamond and is proportional to

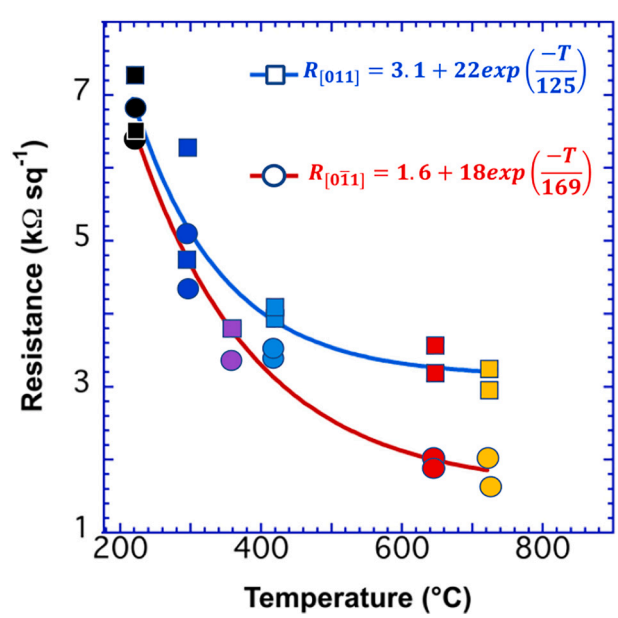

Fig. 4. The surface resistance in the [011] direction, $R_{[011]}$, shown by squares and in the $[0\bar{1}1]$ direction, $R_{[0\bar{1}1]}$, shown by circles as a function of diamond temperature, T. The curves are a fit to the data using equations in the figure. The resistance was calculated from the van-der-Pauw ratio using equations in Appendix C [8]. The Table in Appendix D contains the data for this graph.

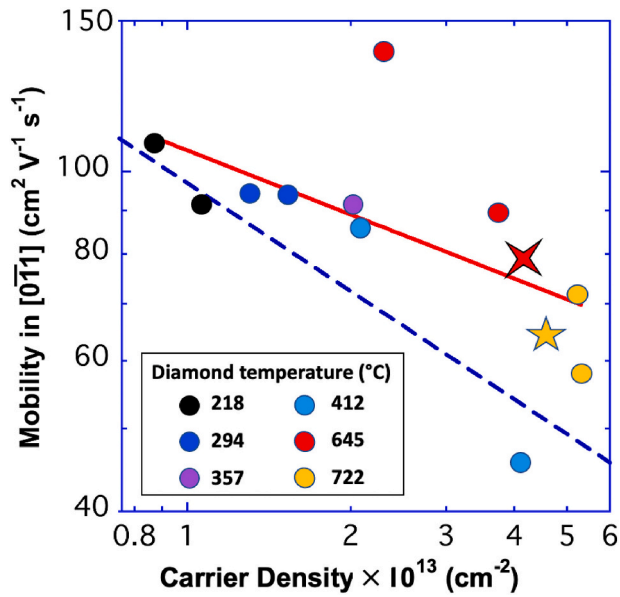

Fig. 5. Carrier mobility in the $[0\bar{1}1]$ direction as function of carrier density. The color of the data points corresponds to the color of the recipes and temperature in Fig. 1. The red curve is a power fit to the data. For comparison the dotted line is a power fit to mobility vs carrier density for air activated diamond [8]. The Table in Appendix D contains the data for this graph.

the -0.42 power of the carrier density [8]. The ALD Al_2O_3/SiO_2 coated diamonds, with few exceptions, give a higher mobility than air activated diamonds with the same carrier density. Fig. 6 shows $R_{[0\bar{1}1]}$ resistance as a function of termination temperature, also shown in Fig. 4, but with error bars and the two nonstandard recipes. The two nonstandard recipes result in resistances that are within the experimental error of diamond terminated at 645 °C, 5 kW. The line curve and equation fit to $R_{[0\bar{1}1]}$ data are shown. The estimated errors for the equation's coefficients were calculated from the data without considering the estimated errors in the actual measurements.

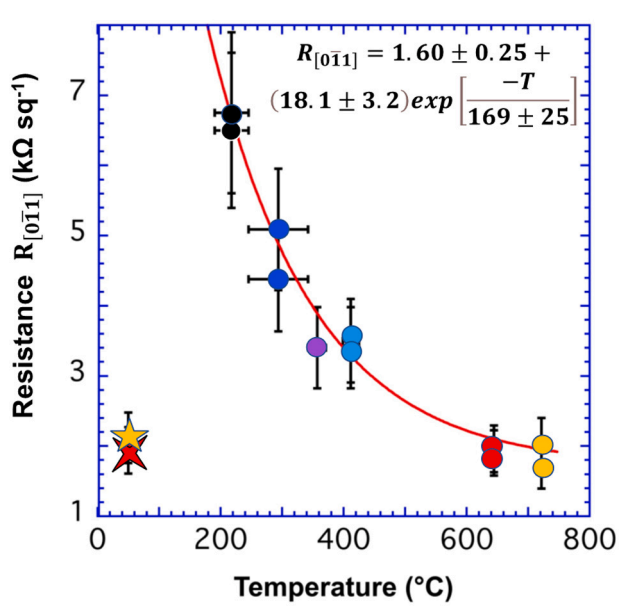

Fig. 6. Resistance along the $[0\bar{1}1]$ direction, $R_{[0\bar{1}1]}$, as a function of diamond temperature. The equation is a fit to the data. The resistances for the two nonstandard recipes are shown by the red four-pointed and yellow five-pointed stars. One of the resistance measurements at 357 °C was not graphed as discussed in the Table in Appendix D.

4. Crystal surface

This work was inspired by Stallcup and Perez's 2001 report [7] on the surface morphology of diamond as a function of substrate temperature during H termination. When the diamond substrate is terminated at 1000 °C, shown in Fig. 7(a), the density of crystal steps is defined by the offcut angle. However, as shown in Fig. 7(b), when terminated at 200 °C the step density increases by more than an order of magnitude and any correlation to the offcut angle is difficult to see. Initially they attributed the differences in surface morphology to anisotropic atomic-H etching at 1000 °C and isotropic etching at 200 °C. However, in a later publication in 2007 [12], they attributed defects and etch pits in the diamond to surface stress generated by dihydride formation where regions on the diamond surface bind two H atoms instead of one for every surface C atom. The dihydride does not form at high temperature, but at temperatures ≤500 °C the dihydride does form. Thoms [13] and Koleske [14] found that even for a diamond at 80 °C atomic H is still reactive on the diamond surface. Y. Yu et al. [15] modeled dihydride structures on diamond and found that troughs or crystal steps in the diamond surface are required to stabilize the dihydride formation over other possible structures.

By changing the H_2 pressure and the microwave plasma power, as reported here, the substrate temperature was varied from 722 to ~218 °C. At high power and temperature we believe the H-terminated diamond surface is like that shown in Fig, 7(a) and at lower powers and temperatures the diamond surface is like that shown in Fig. 7(b). It is speculated that the negative charges in the Al_2O_3/SiO_2 overcoating, which are necessary to generate carriers on the diamond surface, are associated with a specific single step [8], S_B. Examples of which are shown in Fig. 7(a). The lower carrier density obtained with low-power and -temperature termination implies the depletion of the density of steps responsible for surface carriers.

Similar results with H-termination of (100) Si were reported by Boland [16,17] and others [18]. At high temperatures, >335 °C, the surface is similar to Fig. 7(a) and at low temperatures, 33 °C, where the dihydride is stable, the resulting surface is shown in Fig. 8, which is similar to Fig. 7(b). The dihydride generates a confused surface with many steps consisting of mono, di, and trihydrides. For Si the presence of the dihydride also correlates with the etching of the Si surface and at higher temperatures where the dihydride does not form the etching rate of Si was too low to measure [16,17]. Boland reports that the monohydride forms quickly and the dihydride takes minutes as the surface is etched and new crystal steps are generated.

It appears for diamond H-termination there can be two time constants; the time required to H terminate the diamond surface with a monohydride, and at low-temperatures the termination time required for the crystal steps to equilibrate with the surface etching and generate steps to stabilize dihydride formation. The carrier densities and resistances are experimentally the same for a diamond H-terminate for 10 s and another terminated for 4 min and 10 s both with 5-kW of microwave power, 145 Torr of H_2 and at 645 °C. At that power and pressure enough H atoms will impinge on the diamond surface to form a monolayer of H atoms in less than a microsecond. In addition, the 2-min

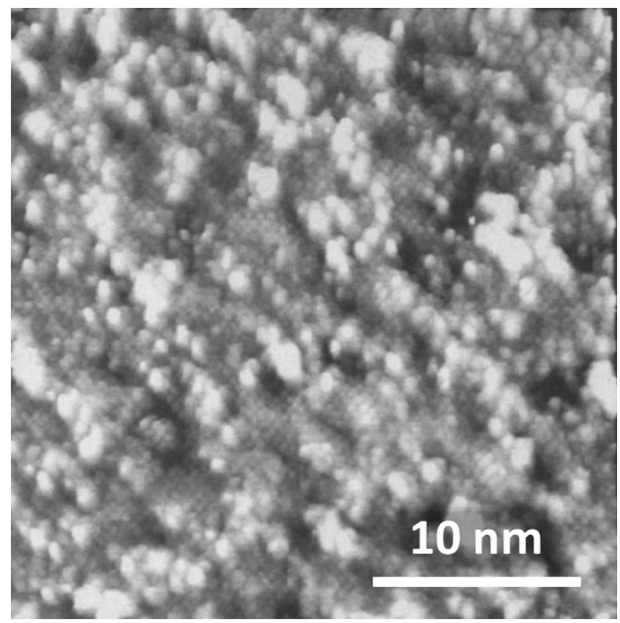

Fig. 8. STM image of the Si(100) surface following a large dose of atomic H at 33 °C [16].
Reprinted with permission from J. J. Boland, Surf. Sci. 261, (1992) 17–28 Copyright 1992, with permission from Elsevier.

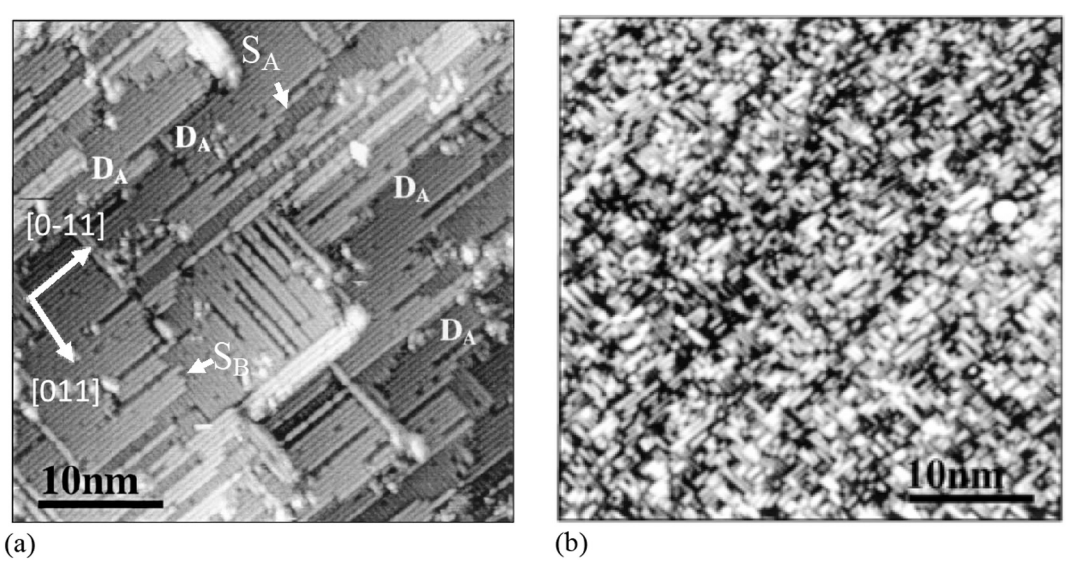

Fig. 7. (a) (100) Scanning tunnel microscope, STM, image of a diamond surface after termination with atomic H for 5 min at 1000 °C [7]. In addition to the 0.089-nm S_A and S_B single crystal steps, double steps, D_A, with a height of 0.18-nm are present. We estimate from the photograph that surface is offcut ~0.6° to toward the [010]. (b) The same or a similar diamond shown in panel (a) after termination at 200 °C for 5 min.
Reprinted with permission from J. M. Perez, Phys. Rev. Lett. 86 (2001) 3368–3371; Copy right 2021 American Physical Society [7].

power ramp down to 0.5 kW and a lower temperature is insufficient time to result in a measurably lower carrier density or higher resistance. Thus the reduced carrier density, shown in Fig. 2, and increased resistance, shown in Fig. 6, is the result of the 2-min soaking at 0.5 kW and not the power ramp from 5 to 0.5 kW. Boland found the same results with Si, where H termination is fast, but at low temperatures it took several minutes for the surface morphology to come to equilibrium with the plasma environment and generate di- and trihydrides [16,17].

When the power and pressure are varied as reported here, the electron and gas temperatures also vary as well as the concentration of atomic H. We are attributing the change in carrier density and resistance to the substrate temperature because of the results of R. E. Stallcup II and J. M. Perez results [7,12].

5. Electrical properties

The surface carrier density is an important parameter determining FETs', maximum drain current, operational voltage, and frequency response. Consider the maximum carrier density for a FET using a gate oxide of Al_2O_3. Although Al_2O_3 can sustain electric fields has high as 30 MV cm^{-1} [19] for practical devices and for gate oxide thickness > 5 nm the maximum operational field is from 5 to 10 MV cm^{-1}. Assuming a dielectric constant of 10 then the maximum carrier density is from 3×10^{13} to 6×10^{13} cm^{-2}. At higher carrier densities, $>6 \times 10^{13}$ cm^{-2}, a depletion mode FET cannot be turned off before the high electric field damages the gate oxide. The maximum carrier density times the saturated velocity from 1×10^7 [20] to 1.4×10^7 cm s^{-1} [21] gives a maximum drain current from 5 to 13 A mm^{-1}. For carrier densities $<1 \times 10^{13}$ cm^{-2} the drain current is limited to <2 A mm^{-1}. The problem in realizing these high current densities is fabricating a FET without degrading the diamond's surface conduction. Fig. 9 shows several published carrier densities as a function of surface resistance for diamond and AlGaN/Ga [22] semiconductors. The carrier densities reported by Todjman [17] and Verona (111) [25] are too high for a depletion mode FETs and Sesame (111)'s density, preprint report, reference 24, is too low, limiting the drain current <1.5 A mm^{-1}. The red curve is the carrier density as a function $R_{[0\bar{1}1]}$ surface resistance for the data presented here.

6. Summary

The diamonds used in these experiments are cutoff 5 to 6° to the [011] axis, which will generate crystal steps that tend to run parallel to the $[0\bar{1}1]$ direction. For diamonds terminated at high temperature the carrier mobility and conductance along the $[0\bar{1}1]$ direction is higher than along the [011] direction. However, for low-temperature termination the resistance is more isotropic, see Fig. 4, as would be expected for the chaotic crystal steps shown in Figs. 7(b) and 8.

The carrier density of H-terminated diamond overcoated with Al_2O_3/SiO_2 can be controllably varied from 1×10^{13} to 6×10^{13} cm^{-2} by controlling diamond temperature during H-termination. In Fig. 1 a diamond that was quenched after 10 s at 5 kW and another diamond ramped from 5 kW to 0.5 kW after 10 s at 5 kW and then quenched, have the same electrical properties to within experimental error as the diamonds H-terminated for 4 min and 10 s at 5 kW, all at 645 °C during termination. This implies that after 10 s at 5 kW that all the diamonds in these experiments were already in a steady state and the power ramp had no measurable effect on the diamond electrical properties. The comparatively short time for a steady-state H-termination is believed due to the high diamond temperature and the efforts to maintain a clean system. It appears that at lower termination powers and temperatures it takes longer to reach a steady state as found for Si by Boland [16,17]. The change in electrical properties is solely due to the 2-min H termination after the power ramp. After repeated H-termination experiments the diamond can become pitted, but empirically this has not affected the electrical results to the level of accurate obtained in these experiments.

From the previous work of Stallcup and Perez [7,12] we believe the change in carrier density is the result of the diamond substrate's temperature during termination. At low temperatures dihydride regions form on the diamond surface during termination. This surface stress generated by the dihydride promotes local etching of the diamond generating new crystal steps. Some of which are shown in Fig. 7(a). There are several kinds of crystal steps that can form each with their own chemical properties [8]. The removal of crystal steps responsible for generating negative surface charge in the Al_2O_3/SiO_2 with lower H-termination temperatures would reduce the carrier density and increase resistance. In spite of the large variation in carrier densities with termination param-

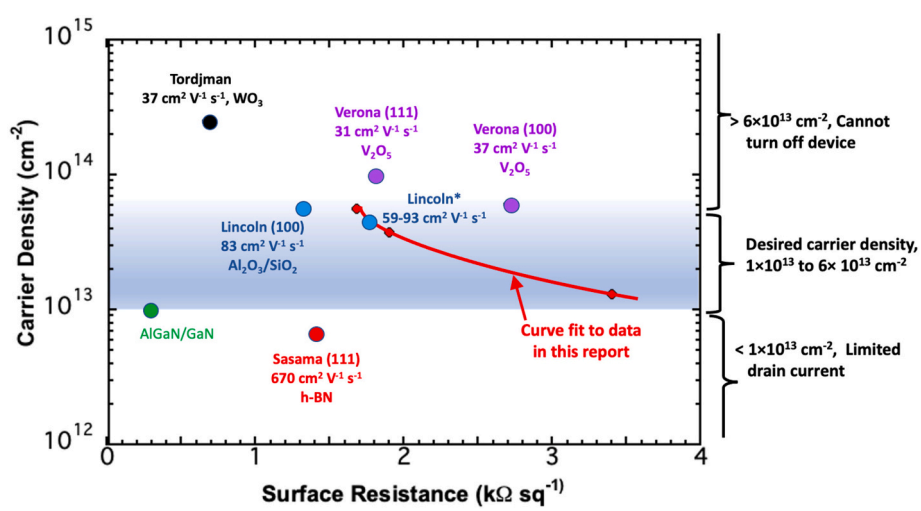

Fig. 9. Graph showing reported surface resistances and carrier densities of H-terminated diamond from the literature and the data reported here. Lincoln* is an average of 10 diamonds. Surface conduction of AlGaN/GaN is shown for comparison. AlGaN/GaN [22], Tordjman [23], Lincoln (100) [8], Sasama (111) [24], and Verona (111) and Verona (100) [25].

eters the mobility is comparatively constant. At present it is unknown what fraction of the diamond surface carbon atoms after H-terminated are terminated with three, two, one, or no H atoms. The techniques, high-resolution electron-energy loss spectroscopy (HREELS [26]) and multiple internal-reflection infrared spectroscopy (MIRIRS [27]), have the potential to determine the density of H and its distribution.

Controlling the carrier density is a requirement to optimize the performance of diamond FETs. At carrier densities $>6 \times 10^{13}$ cm^{-2} FETs cannot be turned off and at densities $<1 \times 10^{13}$ cm^{-2} the maximum drain current is limited to <2 A mm^{-1}, limiting diamond FET performance. In general the carrier density determines the maximum operating voltage, the maximum drain current and the frequency response of a FET and therefore is crucial in determining the FET performance for a specific application.

CRediT authorship contribution statement

M.W. Geis: Conceptualization, Methodology, Software, Data curation, Writing - original draft. M.A. Hollis: Conceptualization, Writing - review & editing. G.W. Turner: Conceptualization, Writing - review & editing. J. Daulton: Conceptualization. J. O. Varghese: Conceptualization. K. Klyukin: review & editing. J. Wang: review & editing. B. Yildiz: Supervision. B. Zhang: Supervision and Editing.

Declaration of competing interest

The authors declare there are no financial interests/personal relationships, which may be considered as potential competing interests.

Acknowledgement

DISTRIBUTION STATEMENT A. Approved for public release. Distribution is unlimited. This material is based upon work supported by the MIT under Air Force Contract No. FA8702-15-D-0001. Any opinions, findings, conclusions or recommendations expressed in this material are those of the author(s) and do not necessarily reflect the views of the MIT.

Appendix A. Hydrogen plasma properties and measurements

Since diamond is not optically opaque between 2 and 2.4 μm, where our optical pyrometer operates, the temperature measurements are inconsistent with the diamonds used in these electrical measurements. To avoid this problem a standard 10 × 10-mm polycrystalline black diamond was used in separate temperature experiments and we assume that under the same conditions the clear diamonds use for electrical measurements were at the same temperature as the standard. Temperatures were measured by an optical pyrometer above 475 °C and below 475 °C the temperature is bracketed by high and low temperature limits, using temperature-indicating lacquers placed on the back of the standard diamond. When the temperature exceeds the lacquer's design temperature the lacquer melts, forming a smooth surface when cooled. If the design temperature is not exceeded the surface of the lacquer remains rough when the diamond is cooled. Fig. A.1 shows the diamond's temperature as a function of plasma power. The average temperature between the high and low measurements is used in the text of the article.

As the microwave power is decreased the plasma changes it character. If the pressure is kept at 145 Torr and the microwave power is decreased the plasma ball moves away from the diamond being H-terminated. At power levels less than 2 kW the plasma is extinguished. To avoid these problems the H_2 pressure was decreased as the microwave plasma power was reduced. The Table below shows the pressures and microwave powers used in this report along with the temperatures and intensities of some selected spectrum lines. The light from the plasma was monitored with an optical fiber and spectrometer looking down through the plasma on to the diamond substrate. The line intensities were measured by recording the light intensity at the specific wavelength and then subtracting the estimated background intensity. The resulting value was then corrected for the spectrometer response. Estimating the electron temperature using the light intensities of Hα and Hβ or determining the H concentration by Ar actinometry [1] is not accurate at the pressures used in this report [2,3]. However some understanding can be obtained from Fig. A.2, showing the spectrum intensity for 6- and 0.5-kW microwave plasma. For the pressures used here, Hα and Hβ light emission is from excited H atoms generated by electron impact on neutral H atoms and Fulcher lines are generated by electron impact on molecular H_2. At low power and pressure, 0.5 kW and 15 Torr, the Fulcher lines are comparable to Hα and Hβ indicating a high percentage of molecular H_2 in the plasma. However, as the power and pressure are increased the plasma ball becomes smaller and the plasma becomes more intense. At 6 kW and 145 Torr the Fulcher lines are barely visible above the background spectrum. Hα and Hβ intensities increase by a factor of ~10 and ~5 respectively with a power increase from 0.5 kW to 6 kW. Indicating that the concentration has H increases at the expense of the H_2 concentration. Similar observations can be made from the molecular emission from 250 to 450 nm, which decreases with increasing power and pressure.

Table
The microwave power and pressure used for H termination. The resulting temperature, atomic intensities of Hα, Hβ, Hγ, and the most intense molecular peak of Fulcher emissions lines are tabulated. The optical intensities are corrected for the spectrometer spectral response.

Microwave power & pressure (kW)/(Torr)	Temperature (°C)	Average temperature (°C)	H_2 pressure (Torr)	Hα intensity 656 nm (arb)	Hβ intensity 486 nm (arb)	Hγ intensity 434 nm (arb)	Fulcher 581 nm (arb)
6.0/145	722	722	145	43,100	2700	240	226
5.0/145	645	645	145	32,500	2070	180	205
3.5/50	399–425	412 ± 13	50	18,300	1390	<100	1030
2.0/40	343–371	357 ± 14	40	12,500	1040	–	1393
1.0/20	246–343	294 ± 48	20	6380	590	–	1250
0.5/15	191–246	218 ± 27	15	4450	400	–	898

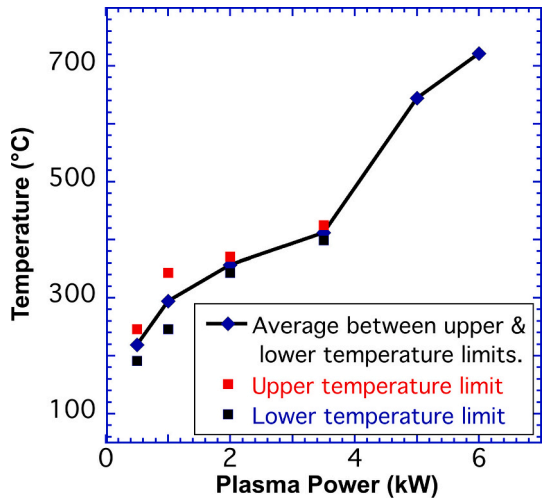

Fig. A.1. Diamond temperature as a function of microwave power. For temperatures above 475 °C an optical pyrometer is used and below 475 °C the temperature is bracket by the highest and lowest temperatures using temperature-indicating lacquers. The average temperature between the highest and lowest limits is also displayed.

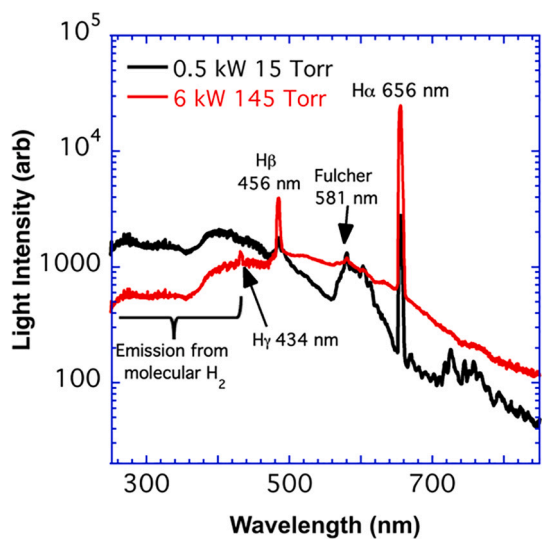

Fig. A.2. Spectrum of emitted light as a function of wavelength for two microwave power levels, 6 kW at 145 Torr and 0.5 kW at 15 Torr. The spectrum is not corrected for spectrometer response.

Appendix B. Atomic layer deposition, ALD

After termination the diamond was overcoated with Al_2O_3/SiO_2 by atomic layer deposition, ALD. The ALD system is preconditioned by heating it to 375 °C and depositing 2 nm of Al_2O_3 using trimethylaluminium (TMA), $Al(CH_3)_3$, and H_2O. Using a load lock the diamond is transferred into the system. After ~4 min, when the diamond is ~150 °C, 1 cycle of H_2O and TMA and 1 cycle of H_2O and BDEA, $Si(N(CH_2CH_3)_2)_4$, are performed. The diamond then heats up to the chamber temperature, 375 °C, over a 20 min period, after which ~18 nm is deposited with 200 cycles of H_2O and TMA.

Appendix C. Resistance measurements

Fig. C1 shows a Hall probe used to measure resistance, carrier density, and mobility. The gold plated clips have no problem contacting through the Al_2O_3/SiO_2 as it poorly adheres to the H-terminated diamond. The resistance between any two clips is ohmic and varied from 8 to 30 kΩ For normal operation a current of 100 μA and a magnetic field of 1 T were used to make these measurements. Mounting and unmounting a diamond several times gave a resistance variation of 3%.

Resistance, carrier density, and mobility were measured on ten diamonds over a period of several months to determine the consistency of these measurements. The diamonds were H-terminated at 6 kW of microwave plasma power and over coated with Al_2O_3/SiO_2 by ALD. Electrical measurements were performed more than 72 h after ALD. The average values with their standard deviation are: resistance 1.77 ± 0.3 kΩ sq^{-1} (±17%), carrier density $4.77 \times 10^{13} \pm 0.72$ (±15%), and mobility 74 ± 9.2 cm^{-2} V^{-1} s^{-1} (±12%).

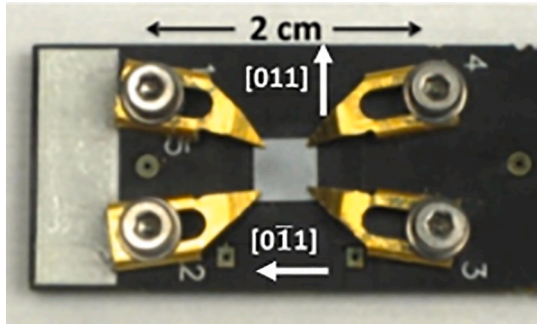

Fig. C1. Photograph of a 4.5 × 4.5 mm diamond mounted for resistance and Hall measurements on a Hall probe. Gold plated clips make ohmic contacts to the diamond. 7 × 7-mm, 0.3-mm thick diamonds were used in these experiments. For this example assume the diamond is mounted with the [0$\bar{1}$1] axis is parallel to the line drawn from clip 2 to clip 3 clip, and the [011] axis is parallel to a line drawn from clip 3 to clip 4.

Basic van-der-Pauw parameters

The clips show in Fig. C1 are numbered 1, 2, 3, and 4. When a current, I_{12}, is passed from clip 1 to clip 2, a voltage, V_{43}, is measured across clips 3 and 4 and the resistance $R_{12,43}$ is defined by abs[V_{12}/I_{43}]. Similarly, $R_{21,34}$ equals abs[V_{21}/I_{34}] with the current flow the in opposite direction, from clip 2 to clip 1. The van-der-Pauw ratio, P_{Ratio} is defined by Eq. (C1).

$$P_{ratio} = \frac{R_{12,34} + R_{21,43} + R_{34,12} + R_{43,21}}{R_{14,32} + R_{41,23} + R_{23,41} + R_{32,14}} \tag{C1}$$

The surface resistance in the [011] direction, $R_{[011]}$ is approximated by Eq. (C2) [4,6] and in the [0$\bar{1}$1] direction $R_{[0\bar{1}1]}$ by Eq. (C3).

$$R_{[011]} \approx R_s P_{ratio}^{0.3} \tag{C2}$$

$$R_{[0\bar{1}1]} \approx R_s P_{ratio}^{-0.3} \tag{C3}$$

where R_S is the van-der-Pauw sheet resistance and is related to the measured parameters R_1 and R_2 by Eq. (C4). R_1 and R_2 are defined by Eqs. (C5) and (C6).

$$e^{-\pi R_1/R_S} + e^{-\pi R_2/R_S} = 1 \tag{C4}$$

$$R_1 = \left(R_{12,34} + R_{34,12} + R_{21,43} + R_{43,21}\right)/4 \tag{C5}$$

$$R_2 = \left(R_{14,32} + R_{32,14} + R_{41,23} + R_{23,41}\right)/4 \tag{C6}$$

Appendix D. Experimental data

The Table of experimental data with sample number, temperatures during termination, microwave power and pressures, van-der-Pauw (VDP) ratios, VPD resistances, resistances in the [0$\bar{1}$1] and the [011] directions, carrier densities and mobilities in the [0$\bar{1}$1] and the [011] directions. Note some diamonds have been used twice, which does not measurably affect the results. The errors for temperature are half the difference between low and

Exp. #	Sample	High temp. (°C)	Low temp. (*C)	Ave. temp. (°C)	Micro. power kΩ	Press. (Torr)	VDP ratio	R_S VDP kΩ	R[0$\bar{1}$1] kΩ	R[011] kΩ	Carrier density (10^{13} cm^{-2})	Mobility [0$\bar{1}$1] (cm^2 V^{-1} s^{-1})	Mobility [011] (cm^2 V^{-1} s^{-1})
1	D302	246	191	218 ± 27	0.5	15	1.01	6.50 ± 1.1	6.50 ± 1.11	6.50 ± 1.11	1.05 ± 0.16	91.2 ± 10.9	91.0 ± 10.9
2	D301	246	191	218 ± 27	0.5	15	1.25	7.00 ± 1.20	6.75 ± 1.14	7.25 ± 1.23	0.86 ± 0.13	106.5 ± 12.8	99.6 ± 12.0
3	D202	343	246	294 ± 48	1	20	1.25	4.59 ± 0.78	4.38 ± 0.74	4.8 ± 0.82	1.53 ± 0.23	90.0 ± 10.8	84.1 ± 10.1
4	D201	343	246	294 ± 48	1	20	1.54	5.62 ± 0.96	5.09 ± 0.87	6.22 ± 1.05	1.31 ± 0.92	76.8 ± 9.2	67.5 ± 8.1
5	D402	371	343	357 ± 14	2	40	1.42	3.59 ± 0.61	3.4 ± 0.58	3.79 ± 0.64	2.01 ± 0.30	91.2 ± 10.9	82.1 ± 9.8
6	D106	371	343	357 ± 14	2	40	1.35	6.52 ± 1.11	6.22 ± 1.06	6.83 ± 1.16	–	–	–
7	D302	425	399	412 ± 13	3.5	50	1.47	3.72 ± 0.63	3.50 ± 0.60	3.95 ± 0.67	2.07 ± 0.31	91.4 ± 11	81.4 ± 9.8
8	D201	425	399	412 ± 13	3.5	50	1.61	3.66 ± 0.62	3.40 ± 0.57	3.94 ± 0.67	4.09 ± 0.61	48.3 ± 5.8	41.8 ± 5.0
9	D102	645	645	645	5	145	4.79	2.50 ± 0.45	1.96 ± 0.32	3.19 ± 0.54	3.04 ± 0.46	106.3 ± 12.8	66.4 ± 8.0
10	D301	645	645	645	5	145	8.05	2.63 ± 0.45	1.90 ± 0.32	3.63 ± 0.62	3.74 ± 0.56	77.9 ± 9.4	41.7 ± 5.0
11	D202	722	721	722	6	145	6.23	2.24 ± 0.38	1.68 ± 0.29	2.98 ± 0.51	5.57 ± 0.84	63.7 ± 7.6	36.8 ± 4.4
12	D104	722	721	722	6	145	4.5	2.59 ± 0.44	2.05 ± 0.35	3.28 ± 0.56	5.31 ± 0.80	71.9 ± 8.6	45.8 ± 5.5
13	D106 quench	–	–	–	0	–	4.61	2.77 ± 0.47	1.94 ± 0.33	3.95 ± 0.67	4.11 ± 0.61	98.6 ± 11.8	62.3 ± 7.5
14	D301 ramp	–	–	–	5 to 0.5	145 to 15	2.57	2.44 ± 0.41	2.12 ± 0.36	2.81 ± 0.48	4.62 ± 0.69	63.9 ± 7.7	48.2 ± 5.8

high temperatures in the table. The resistance, carrier density, and mobility errors are estimates from previous measurements discussed in Appendix C, ±17% for resistance, ±15% for carrier density, and ±12% for mobility. The results of experiment 6, D106 at 357 °C, were not used in the analysis as the Hall measurements were not reproduceable and noisy and the resistance is substantially above the measured resistance of experiments 3, 4, same experimental condition 5, 6 and 7.

References

[1] Z.-C. Geng, Y. Xu, X.-F. Yang, W.-G. Wang, A.-M. Zhu, Atomic hydrogen determination in medium-pressure microwave discharge hydrogen plasmas via emission actinometry, Plasma Sources Sci. Technol. 14 (2005) 76–82, https://doi.org/10.1088/0963-0252/14/1/010.

[2] E.J.D. Mahoney, B.S. Truscott, S. Mushtaq, M.N.R. Ashfold, Y.A. Mankelevich, Spatially resolved optical emission and modeling studies of microwave-activated hydrogen plasmas operating under conditions relevant for diamond chemical vapor deposition, J. Phys. Chem. A 122 (2018) 8286–8300, https://doi.org/10.1021/acs.jpca.8b07491.

[3] E.J.D. Mahoney, S. Mushtaq, M.N.R. Ashfold, Y.A. Mankelevich, Combined spatially resolved optical emission imaging and modeling studies of microwave- activated H2/Ar and H2/Kr plasmas operating at powers and pressures relevant for diamond chemical vapor deposition, J. Phys. Chem. A 123 (2019) 2544–2558, https://doi.org/10.1021/acs.jpca.8b12294.

[4] M.W. Geis, J.O. Varghese, J. Alon Vardi, J. Kedzierski, D. Daulton, M.A. Calawa, C. H. Hollis, G.W. Wuorio, S.M. Turner, T. Warnock, J. Osadchy, A.Melville Mallek, A. del Jesus, B.Zhang Alamo, Hydrogen and deuterium termination of diamond for low surface resistance and surface step control, Diam. Relat. Mater. 118 (2021), 108518, https://doi.org/10.1016/j.diamond.2021.108518.

[5] I. Miccoli, F. Edler, H. Pfnur, C. Tegenkamp, The 100th anniversary of the four- point probe technique: the role of probe geometries in isotropic and anisotropic systems, J. Phys. Condens. Matter 27 (2015), 223201, https://doi.org/10.1088/0953-8984/27/22/223201.

[6] H.C. Montgomery, Method for measuring electrical resistivity of anisotropic materials, J. Appl. Phys. 42 (1971) 2971–2975, https://doi.org/10.1063/1.1660656.

References

[1] M.I. Landstrass, K.V. Ravi, Resistivity of chemical vapor deposited diamond films, Appl. Phys. Lett. 55 (1989) 975–977, https://doi.org/10.1063/1.101694.

[2] F. Maier, M. Riedel, B. Mantel, J. Ristein, L. Ley, Origin of surface conductivity in diamond, Phys. Rev. Lett. 85 (2000) 3472–3475, https://doi.org/10.1103/PhysRevLett.85.3472.

[3] K.G. Crawford, I. Maini, D.A. Macdonald, D.A.J. Morgan, Surface transfer doping of diamond: a review, Prog. Surf. Sci. 96 (2021), 100613, https://doi.org/10.1016/j.progsurf.2021.100613.

[4] M.W. Geis, C.H. Wuorio, T.H. Fedynyshyn, B. Duncan, M.E. Plaut, J.O. Varghese, S. M. Warnock, S.A. Vitale, M.A. Hollis, T.C. Wade, Progress toward diamond power field-effect transistors, Phys. Status Solidi A 215 (2018), 1800681, https://doi.org/10.1002/pssa.201800681.

[5] Z. Chen, Y. Fu, H. Kawarada, Y. Xu, Microwave diamond devices technology: field-effect transistors and modeling, Numer. Model. 3 (2021), e2800, https://doi.org/10.1002/jnm.2800.

[6] N.C. Saha, S.-W. Kim, T. Oishi, Y. Kawamata, K. Koyama, M. Kasu, 345-MW/cm^2 2608-V NO_2 p-Type doped diamond MOSFETs with an Al_2O_3 passivation overlayer on heteroepitaxial diamond, IEEE Electron Dev. Lett. 42 (2021) 903–906, https://doi.org/10.1109/LED.2021.3075687.

[7] R.E. Stallcup II, J.M. Perez, Scanning tunneling microscopy studies of temperature-dependent etching of diamond (100) by atomic hydrogen, Phys. Rev. Lett. 86 (2001) 3368–3371, https://doi.org/10.1103/PhysRevLett.86.3368.

[8] M.W. Geis, J.O. Varghese, J. Alon Vardi, J. Kedzierski, D. Daulton, M.A. Calawa, C. H. Hollis, G.W. Wuorio, S.M. Turner, T. Warnock, J. Osadchy, A.Melville Mallek, A. del Jesus, B.Zhang Alamo, Hydrogen and deuterium termination of diamond for low surface resistance and surface step control, Diam. Relat. Mater. 118 (2021), 108518, https://doi.org/10.1016/j.diamond.2021.108518.

[9] M.W. Geis, J.O. Varghese, M.A. Hollis, R.J. Nemanich, X. Zhang, G.W. Turner, S. M. Warnock, S.A. Vitale, T. Osadchy, B. Zhang, Stable, low-resistance, 1.5 to 3.5 kΩ sq^{-1}, diamond surface conduction with a mixed metal-oxide protective film, Diam. Relat. Mater. 106 (2020), 107819, https://doi.org/10.1016/j.diamond.2020.107819.

[10] I. Miccoli, F. Edler, H. Pfnur, C. Tegenkamp, The 100th anniversary of the four-point probe technique: the role of probe geometries in isotropic and anisotropic systems, J. Phys. Condens. Matter 27 (2015), 223201, https://doi.org/10.1088/0953-8984/27/22/223201.

[11] H.C. Montgomery, Method for measuring electrical resistivity of anisotropic materials, J. Appl. Phys. 42 (1971) 2971–2975, https://doi.org/10.1063/1.1660656.

[12] R.E. Stallcup II, Y. Mo, T.W. Scharf, J.M. Perez, Formation of nanometer-size high-density pits on epitaxial diamond (100) films, Diam. Relat. Mater. 16 (2007) 1727–1731, https://doi.org/10.1016/j.diamond.2007.06.001.

[13] B.D. Thoms, J.N. Russell Jr., P.E. Pehrsson, J.E. Butler, Adsorption and abstraction of hydrogen on polycrystalline diamond, J. Chem. Phys. 100 (1994) 8425–8431, https://doi.org/10.1063/1.466740.

[14] D.D. Koleske, S.M. Gates, B.D. Thoms, J.N. Russell Jr., J.E. Butler, Hydrogen on polycrystalline diamond films: studies of isothermal desorption and atomic deuterium abstraction, J. Chem. Phys. 102 (1995) 992–1002, https://doi.org/10.1063/1.469167.

[15] Y. Yu, C.Z. Gu, L.F. Xu, S.B. Zhang, Ab initio structural characterization of a hydrogen-covered diamond (001) surface, Phys. Rev. B 70 (2004), 125423, https://doi.org/10.1103/PhysRevB.70.125423.

[16] J.J. Boland, Role of bond-strain in the chemistry of hydrogen on the Si (100) surface, Surf. Sci. 261 (1992) 17–28, https://doi.org/10.1016/0039-6028(92)90214-Q.

[17] J.J. Boland, Scanning tunnelling microscopy of the interaction of hydrogen with silicon surfaces, Adv. Phys. 42 (1993) 129–171, https://doi.org/10.1080/00018739300101474.

[18] H.N. Waltenburg, J.T. Yates Jr., Surface chemistry of silicon, Chem. Rev. 95 (1995) 1589–1673. https://pubs.acs.org/doi/pdf/10.1021/cr00037a600.

[19] H.C. Lin, P.D. Ye, Leakage current and breakdown electric-field studies on ultrathin atomic-layer-deposited Al_2O_3 on GaAs, Appl. Phys. Lett. 87 (2005), 182904.

[20] S. Imanishi, K. Horikawa, N. Oi, S. Okubo, T. Kageura, A. Hiraiwa, H. Kawarada, 3.8 W/mm RF power density for ALD Al_2O_3-based two-dimensional hole gas diamond MOSFET operating at saturation velocity, IEEE Electron Device Lett. 40 (2019) 279–282, https://doi.org/10.1109/LED.2018.2886596.

[21] J.Y. Tsao, S. Chowdhury, M.A. Hollis, D. Jena, N.M. Johnson, K.A. Jones, R. J. Kaplar, S. Rajan, C.G. Van de Walle, E. Bellotti, C.L. Chua, R. Collazo, M. E. Coltrin, J.A. Cooper, K.R. Evans, S. Graham, T.A. Grotjohn, E.R. Heller, M. Higashiwaki, M.S. Islam, P.W. Juodawlkis, M.A. Khan, A.D. Koehler, J.H. Leach, U.K. Mishra, R.J. Nemanich, R.C.N. Pilawa-Podgurski, J.B. Shealy, Z. Sitar, M. J. Tadjer, A.F. Witulski, M. Wraback, J.A. Simmons, Ultrawide-bandgap semiconductors: research opportunities and challenges, Adv. Electron. Mater. 4 (2018), 1600501, https://doi.org/10.1002/aelm.201600501.

[22] T.-S. Ko, D.-Y. Lin, C.-F. Lin, C.-W. Chang, J.-C. Zhang, S.-J. Tud, High-temperature carrier density and mobility enhancements in AlGaN/GaN HEMT using AlN spacer layer, J. Crystal Growth 464 (2017) 175–179, https://doi.org/10.1016/j.jcrysgro.2016.12.023.

[23] M. Tordjman, R. Kalish, Boosting surface charge-transfer doping efficiency and robustness of diamond with WO_3 and ReO_3, Appl. Phys. Lett. 111 (2017), 111601, https://doi.org/10.1063/1.4986339.

[24] Y. Sasama, T. Kageura, M. Imura, K. Watanabe, T. Taniguchi, T. Uchihashi, Y. Takahide, High-Mobility p-Channel Wide Bandgap Transistors Based on h-BN/Diamond Heterostructures, arXiv.org, cond-mat, arXiv:2102.05982, 2021. https://arxiv.org/abs/2102.05982.

[25] C. Verona, F. Arciprete, M. Foffi, E. Limiti, M. Marinelli, E. Placidi, G. Prestopino, G.V. Rinati, Influence of surface crystal-orientation on transfer doping of V_2O_5/H-terminated diamond, Appl. Phys. Lett. 112 (2018), 181602, https://doi.org/10.1063/1.5027198.

[26] B.D. Thorns, P.E. Pehrsson, J.E. Butler, A vibrational study of the adsorption and desorption of hydrogen on polycrystalline diamond, J. Appl. Phys. 75 (1994) 1804–1810, https://doi.org/10.1063/1.356373.

[27] B.F. Mantel, M. Stammler, J. Ristein, L. Ley, The correlation between surface conductivity and adsorbate coverage on diamond as studied by infrared spectroscopy, Diam. Relat. Mater. 10 (2001) 429–433, https://doi.org/10.1016/S0925-9635(00)00601-4.